

Direct simulations of spherical particles sedimenting in viscoelastic fluids

N. Goyal & J.J. Derksen*

Chemical & Materials Engineering, University of Alberta, Edmonton, Alberta, T6G 2G6 Canada,

*email: jos@ualberta.ca

Submitted to J Non-Newtonian Fluid Mech., April 2012

Revision submitted: June 2012

2nd revision submitted: July 2012

Accepted: July 2012

Abstract

A direct simulation methodology for solid spheres moving through viscoelastic (FENE-CR) fluids has been developed. It is based on a lattice-Boltzmann scheme coupled with a finite volume solver for the transport equation of the conformation tensor, which directly relates to the elastic stress tensor. An immersed boundary method imposes no-slip conditions on the spheres moving over the fixed grid. The proposed method has been verified by comparison with computational data from the literature on the viscoelastic flow past a stationary cylinder. Elastic effects manifest themselves in terms of drag reduction and fore-aft asymmetry around the cylinder. Single sphere sedimentation in viscoelastic fluids shows velocity overshoots and subsequent damping before a steady settling state is reached. In multi-sphere simulations, the interaction between spheres depends strongly on the (elastic) properties of the liquid. Simulations of sedimentation of multiple spheres illustrate the potential of the method for application in dense solid-liquid suspensions. The sedimentation simulations have Reynolds numbers of order 0.1 and Deborah numbers ranging from 0 to 1.0.

Keywords

Viscoelastic fluid, lattice-Boltzmann, finite volume, immersed boundary method, hindered settling, FENE-CR

Introduction

Solid particles settling in liquid under the influence of gravity is a topic of research with a long and rich tradition [1-3], continuing interest [4,5], and significant practical relevance. Where the research cited above deals with Newtonian liquids, practical relevance also demands considering solid particles in liquid with more complex rheological behavior. Applications of this sort can be found in such diverse fields as oil sands mining, foods, pharmaceuticals, and personal care products. In the latter examples one can think of solid particles that need to stay dispersed (i.e. not settle) in a gel-type continuous liquid phase. In oil sands mining, surface active clays in water-rich environments form soft networks that behave as yield-stress and/or elastic liquids. Coarser (sand) particles suspended in such liquids only settle very slowly (or not at all) making e.g. gravity-based separations a lengthy and inefficient process.

Numerical simulations are a way to gain understanding of the behavior of solid-liquid suspensions, including those with non-Newtonian liquid rheology. Such numerical simulations come in a great variety. What distinguishes them is their level of detail on one side, and the size of the systems they are capable of handling on the other. The numerical approaches proposed here deal with fully resolved simulations. In such simulations the flow structures are resolved down to scales smaller than the particles size. This allows for the direct determination of the hydrodynamic forces and torques on the particles that – in turn – determine their (linear and rotational) motions. The latter are fed back to the liquid flow as moving, no-slip boundary conditions. The price for solving that much detail is that it is only possible to simulate a limited number of particles (up to order 10^4 , as in [6,7]) in a small sample, and we cannot capture overall behavior of macro-scale processes.

Our ambition is to develop a method for performing highly resolved simulations of dense (i.e. high solids volume fraction) suspensions of solid particles in viscoelastic liquids. In such suspensions, solids and liquid interact in multiple ways: solids directly interact through collisions, and they interact through the interstitial liquid. The solids motion also drives liquid flow, and vice versa. It is expected that the viscoelastic rheology of the liquid has profound impact on the dynamics of the suspension as a whole. The

numerical procedure is based on the lattice-Boltzmann method for solving the flow of interstitial liquid, and an immersed boundary method for imposing the no-slip condition at the moving solid-liquid interfaces. This fixed-grid approach makes it possible to computationally efficiently simulate many-particle systems. Previous work on suspensions with Newtonian liquids has shown favorable agreement with experimental data [7,8] and has demonstrated the usefulness of understanding interactions in dense suspensions e.g. under turbulent conditions [9], during erosion of granular beds [10], and with systems in which the solids have a tendency to aggregate [11]. The specific lattice-Boltzmann scheme applied in this study [12] explicitly deals with (among more) stresses as part of the solution vector which facilitates incorporation of an additional elastic stress in the scheme. Although particle-based Reynolds numbers in most non-Newtonian applications are (very) small, the numerical method is able to also deal with suspensions showing inertial effects.

The purpose of this paper is to establish the numerical approach by performing a number of benchmark simulations involving flow of viscoelastic liquids around objects in two and in three dimensions and comparing results with what is known from the literature, thereby assessing accuracy – including the effects of grid resolution. In addition, by performing simulations with multiple, spherical particles (up to eight in this paper) we provide a “proof of concept” before moving on to bigger and denser systems in the near future. The liquids used in this work are all based on the Chilcott and Rallison's finite extension (FENE-CR) model [13].

Pioneering experimental work on hydrodynamic interaction between spherical particles in viscoelastic liquids is due to Riddle et al [14], Joseph et al [15], and Bot et al [16]. Simulations in two dimensions involving multiple particles settling through viscoelastic liquid date back to the work by Feng et al in 1996 [17], showing interesting phenomena such as velocity overshoot, and preferential orientations. More recent two-dimensional work with (many) more circular particles has been reported by Hao et al [18], Yu et al [19], and Singh et al [20]. Simulations of spherical particle motion through viscoelastic liquids are restricted to one or two spheres: Bodart & Crochet [21] (one sphere, two-

dimensional, axisymmetric simulations), Binous & Phillips [22] (up to two spheres, three-dimensional), and (more recently) Villone et al [23] (one sphere, three-dimensional).

This paper is organized in the following manner: first the FENE-CR model is outlined with a focus on the equations that need to be solved numerically to provide the temporal and spatial evolution of the elastic stress tensor. With the four liquid parameters associated with the FENE-CR model, along with flow conditions we establish a set of dimensionless numbers. Then we show how the lattice-Boltzmann method has been coupled to a finite volume method with the latter solving for the elastic stress tensor. This section includes a discussion of the boundary conditions. As a first benchmark the two-dimensional flow of FENE-CR liquid past a cylinder placed in a channel has been considered. Then we move to three-dimensional simulations; first with a single spherical particle, then with two spherical particles with a focus on their hydrodynamic interaction. Finally we demonstrate the feasibility of performing multiple-particle simulations. At the end we summarize and reiterate the main conclusions.

Physical and numerical formulation

Viscoelasticity model

In this study the Chilcott and Rallison's finite extension (FENE-CR) model [13] was used. Based on molecular theory, the FENE-CR model represents the fluid elasticity by an ensemble average of dumbbells immersed in a Newtonian fluid. Such a dumbbell consists of two beads and an elastic interconnect (spring). The elastic effects are due to the action of the spring's force and the momentum exchange between the dumbbell and the Newtonian fluid. The total stress $\boldsymbol{\sigma}$ has a pressure contribution ($P\mathbf{I}$), a viscous stress contribution ($\boldsymbol{\tau}^s$), and an elastic stress contribution ($\boldsymbol{\tau}^e$):

$$\boldsymbol{\sigma} \equiv -P\mathbf{I} + \boldsymbol{\tau}^s + \boldsymbol{\tau}^e \quad (1)$$

with $\boldsymbol{\tau}^s = \mu_s \left(\nabla \mathbf{u} + (\nabla \mathbf{u})^T \right)$ and \mathbf{u} the velocity field. The Newtonian 'solvent' viscosity is recognized as μ_s .

In the FENE-CR model the elastic stress is

$$\boldsymbol{\tau}^e = \frac{\mu_p}{\lambda} F(\mathbf{A})(\mathbf{A} - \mathbf{I}) \quad (2)$$

with $\mathbf{A} = \langle \mathbf{RR} \rangle$ the ensemble-average dyadic product of dumbbell orientation \mathbf{R} , and the scalar function F the spring force function $F(\mathbf{A}) = \frac{1}{1 - \text{tr}(\mathbf{A})/L^2}$. The three elastic material parameters μ_p , λ , and L can be interpreted as the elastic contribution to the shear viscosity, the relaxation time, and the maximum spring extension length respectively. The tensor \mathbf{A} obeys the following transport equation

$$\frac{\partial \mathbf{A}}{\partial t} + \mathbf{u} \cdot \nabla \mathbf{A} = \mathbf{A} \cdot \nabla \mathbf{u} + (\nabla \mathbf{u})^T \cdot \mathbf{A} - \frac{F(\mathbf{A})}{\lambda} (\mathbf{A} - \mathbf{I}). \quad (3)$$

The FENE-CR model recovers the Oldroyd-B model [24] in the limiting case of $L^2 \rightarrow \infty$. Both FENE-CR and Oldroyd-B are constant viscosity models. The application of Oldroyd-B fluids is limited because it allows (unphysical) infinite dumbbell extension.

Dimensionless numbers

Where many systems involving Newtonian fluid flow can be pinned down by the flow geometry (in terms of aspect ratios) and the Reynolds number, the four material parameters in the FENE-CR model (μ_s , μ_p , λ , and L) give rise to a parameter space with more dimensionless numbers. With our application of sedimentation of spherical particles (with diameter d and density ρ_s) in mind, results will generally be presented in the following non-dimensional form

$$\frac{\lambda U}{d} = f \left[\frac{\lambda \mu_0}{\rho d^2}, \frac{g \lambda^2}{d}, \frac{\mu_s}{\mu_0}, \frac{\rho_s}{\rho}, L, \text{aspect ratios} \right], \quad (4)$$

with the characteristic velocity U (e.g. the settling velocity) as an output parameter on the left-hand side, and the input parameters on the right. The liquid density is identified as ρ , g is gravitational acceleration,

and $\mu_0 \equiv \mu_s + \mu_p$. The Deborah number is recognized as $\text{De} = \frac{\lambda U}{d}$, the elasticity number as $\text{El} = \frac{\lambda \mu_0}{\rho d^2}$, the

gravity parameter as $G = \frac{g\lambda^2}{d}$, and the viscosity ratio as $\beta = \frac{\mu_s}{\mu_0}$. The parameter L is non-dimensional; it

represents the ratio of the maximum extension length of a dumbbell divided by its equilibrium length. The

Reynolds number can be written as $\text{Re} = \frac{\text{De}}{\text{El}} = \frac{\rho U d}{\mu_0}$.

In addition to the above, settling velocities in viscoelastic liquids will also be compared to the

Stokes settling velocity U_∞ according to $U_\infty = \frac{(\rho_s - \rho)gd^2}{18\mu_0}$, and $\text{Re}_\infty = \frac{\rho U_\infty d}{\mu_0}$.

Numerical approach

The basis of our numerical approach is formed by a lattice-Boltzmann (LB) flow solver according to the scheme proposed by Somers [12]. An LB fluid can be viewed as a collection of fluid parcels residing on a uniform, cubic lattice with grid spacing Δ . Each time step these parcels stream to neighboring lattice sites where they collide (i.e. exchange momentum) with parcels coming from other directions to the same site.

The state of the flow at discrete moment t in time and discrete location \mathbf{x} in space is defined by the distribution of the mass of the fluid parcels over the discrete set of velocities in the lattice $N_i(\mathbf{x}, t)$. The index i relates to the discrete set of velocities \mathbf{c}_i ($i=1\dots 18$ directions in our approach). The set of velocities

is discrete given the uniformity of the lattice and the fact that parcels are only allowed to move to neighboring lattice sites during one time step. Macroscopic flow variables follow from summing mass and

momentum per lattice site: $\rho(\mathbf{x}, t) = \sum_{i=1}^{18} N_i(\mathbf{x}, t)$, $\rho\mathbf{u}(\mathbf{x}, t) = \sum_{i=1}^{18} \mathbf{c}_i N_i(\mathbf{x}, t)$. Pressure is linked to density

through an equation of state. The grid spacing and time step are taken as unit length and time respectively:

$\Delta = 1$ and $\Delta t = 1$.

In the LB scheme due to Somers [12], the streaming step is performed in terms of N_i ; the collision step, however, is performed in terms of the macroscopic flow variables: density (scalar), momentum (vector), and stress (tensor). This allows for directly adding the elastic stress to the pressure and viscous

stress already present in the LB momentum balance. After initialization with zero velocity, zero stress and uniform density, the flow systems are evolved in time in the following manner: First the transport equation for the tensor \mathbf{A} (Eq. 3) is solved according to an explicit finite volume (FV) scheme (more details below). This allows us to determine the elastic stress tensor according to Eq. 2. We then perform an LB time step in the same manner as we would do for a Newtonian fluid, only now with the additional elastic stress $\boldsymbol{\tau}^e$. This LB step provides us with an updated velocity field \mathbf{u} that is used to perform the next FV time step to update $\boldsymbol{\tau}^e$, and so on.

We chose to solve the transport equations in the components of \mathbf{A} with a FV scheme and not in an LB manner (as e.g. done by Malaspinas et al [25]) since – at least in our explicit formulation – FV methods are less memory intensive and have the same parallelization potential as LB schemes. In addition FV methods have well-developed options for controlling numerical diffusion [26].

The FV approach for solving Eq. 3 uses the same uniform, cubic grid and the same time step as used by the LB scheme. Since \mathbf{A} is symmetric, each time step the six independent components $A_{\alpha\beta}$ (with α and β the coordinate directions) are updated. The update is Euler explicit, so that the right-hand side of Eq. 3 is treated as a (known) source term at the old time level, except for the term $\frac{F(\mathbf{A})}{\lambda}\mathbf{A}$. To enhance stability the latter term is transferred to the left-hand side if $F(\mathbf{A}) > 0$ so that \mathbf{A} (not $F(\mathbf{A})$ though) is represented at the new time level. The convective fluxes in Eq. 3 have been discretized as a blend between first-order upwind difference, and second-order central difference [27] with a weighing factor of 0.9 towards the central difference giving stable behavior of the FV solver.

Boundary conditions

No-slip conditions at the walls bounding the rectangular flow domains are dealt with by means of the half-way bounce back rule, where fluid parcels N_i reverse direction when they hit a wall and return to the lattice site they started from at the beginning of the time step [28]. This places the wall at distance $\Delta/2$

from lattice nodes adjacent to the wall. Inflow and outflow boundary conditions are based on a zero normal-gradient approach which implies copying fluid parcel populations N_i in the streamwise direction at inflow and outflow and imposing a velocity profile at an inflow boundary [29].

Curved and/or moving no-slip walls inside the flow domain (as we have when studying particle sedimentation) are imposed by an immersed boundary (IB) method [30,31]. As these boundary conditions are in terms of velocity (not in terms of stress) we use the same approach as we have been using extensively for solid-liquid suspensions with Newtonian fluids [7,9,10]. In this approach the solid surface is defined by a set of closely spaced points not coinciding with the lattice; the typical spacing between points is 0.7Δ . The fluid velocity at these points is determined by interpolation from the lattice. A control algorithm based on locally forcing the fluid [30] is applied to match the local fluid velocity with the velocity of the (moving) solid surface. A consequence of this methodology is that the particles have internal fluid and thus internal (elastic) stress. The internal stress has no physical meaning. Its presence, however, could have impact on resolving stress and (steep) stress gradients in the fluid near the particle surface. The latter has been tested through comparison with results of simulations from the literature, and through grid refinement studies (see the next section).

The force distribution around the solid surface of a particle is integrated to determine the total force and torque the particle exerts on the fluid. The opposite (action is minus reaction) are the force and torque exerted on the particle by the fluid. These we use to update the equations of (linear and rotational) motion of the particle in which the time derivatives (i.e. the accelerations) are discretized according to a second-order two-level backward difference scheme: for a velocity component w_α that depends on time we write

$$\frac{dw_\alpha}{dt} \approx \frac{3w_\alpha^{(n+1)} - 4w_\alpha^{(n)} + w_\alpha^{(n-1)}}{2\Delta t}$$

with n the current time level (at which force and torque have been evaluated), and $n+1$ and $n-1$ the new and old time levels respectively.

The set of points defining the spherical surface moves with the particle over the fixed and uniform lattice. This provides a way to efficiently deal with many particles. The flip side is that grids are not locally

refined in high-gradient regions (e.g. between two closely spaced spheres), and these resolution limitations of our numerical method need to be carefully assessed.

The hyperbolic (i.e. non-diffusive) nature of the transport equation in \mathbf{A} (Eq. 3) makes that we do not need elastic stress boundary condition at solid walls and at outflow boundaries. At inflow boundaries the elastic stress distribution has been determined analytically based on the specified inlet velocity profile.

Benchmark: two-dimensional flow past a cylinder

As a benchmark case we consider the two-dimensional viscoelastic flow past a cylinder that is placed in the center of a plane channel, see Figure 1 for the definition of the flow geometry and the associated coordinate system. This flow has been studied experimentally by Verhelst & Nieuwstadt [32], and computationally by Alves et al [33], and by Fan et al [34]. The results due to Alves et al will be used for comparison with our simulation results.

The parabolic (Poiseuille) velocity profile is imposed at the inlet along with the conformation tensor \mathbf{A} associated with this velocity profile and the assumption the flow has fully developed upstream of the inlet boundary. A zero-normal-gradient condition for velocity is imposed at the outlet. By extending the length of the domain we confirmed that the domain is sufficiently long for the location of the outflow to have no effect on the simulation results. The no-slip (zero velocity) condition completely characterizes the channel walls and no additional conditions are required there for the elastic stress.

The cylinder is represented by the immersed boundary method. As the characteristic length and velocity we take the cylinder radius $R=D/2$ and the average fluid velocity at the channel inlet U respectively (the average velocity and center line velocity U_{CL} are related according to $U = 2U_{CL}/3$). This defines a Reynolds number that has been fixed to $Re=0.067$. Also the blockage ratio has been fixed:

$Br \equiv \frac{R}{H} = 0.25$. Results will be presented in the form of velocity and stress profiles and in terms of the drag

coefficient. To be consistent with the literature [33], the latter has been defined as $C_d \equiv \frac{F_d}{\mu_0 U}$ with F_d the

force exerted by the flow on the cylinder. The drag force follows from integrating the forces calculated by the IB method to maintain no-slip over the cylinder surface.

Results on three meshes will be compared; mesh M1, M2, and M3 have a lattice spacing Δ such that $R = 5\Delta, 10\Delta$, and 15Δ respectively. Figure 2 shows centreline and wall-normal profiles of the streamwise velocity. There are minor differences between the M2 and M3 results for a Newtonian liquid, as well as for an Oldroyd-B liquid. If the two liquids are compared it is observed that the elastic liquid has a longer wake, and that it accelerates faster when passing through the gap between the cylinder and the channel wall. These observations regarding the flow will be further detailed below.

Our results can be directly compared to the numerical results due to Alves et al [33] for Oldroyd-B fluids. There are only slight differences in the input parameters and flow configuration: In their study $Re=0$, the viscosity ratio is $\beta = 0.59$, and the channel length is $L_{ch} = 60R$; we have $Re=0.067$, $\beta = 0.60$, and $L_{ch} = 40R$. The rest of the input parameters are the same. In what follows we will focus on the effect of the Deborah number on the flow around the cylinder and the drag force on the cylinder.

Table 1 here

Table 1 and Figure 3 summarize our results regarding the drag coefficient in relation to Alves et al's [33] data. The table shows adequate grid convergence from mesh M2 to mesh M3. The trends in the drag coefficient versus the Deborah number are well captured by our simulation method: a decay in C_d until $De=0.6$ after which C_d levels off and marginally increases beyond $De = 0.8$. Our drag coefficients are systematically some 2 to 3% higher than Alves et al's [33]. We attribute this to the cylinder being represented on a square grid. As will be discussed in the next section (on three-dimensional flows) an increased hydrodynamic force on curved surfaces in square grids is a known effect that – to a large extent – can be corrected for.

Profiles of the axial velocity along the channel centerline for $De=0.0, 0.6$, and 0.9 are presented in Figure 4. At this low Reynolds number ($Re=0.067$) the Newtonian case ($De=0$) is approximately fore-aft symmetric. For the viscoelastic fluids this symmetry is progressively distorted with increasing elasticity.

The perturbation length downstream of the cylinder increases with increasing Deborah number. Upstream of the cylinder, the velocity is not significantly affected by elasticity and the profiles virtually overlap. Figure 4 also contains results due to Alves et al [33] with a good agreement between their and our data.

Profiles of the elastic normal xx -stress along the centerline at $De = 0.6, 0.7$ and 1.0 are plotted in Figure 5. The peak stress levels directly downstream of the cylinder are a strong function of the Deborah number, with very high stress gradients in the near wake where liquid elongates rapidly. Capturing this structure accurately requires high spatial resolution, as recognized in [33]. In Figure 5 it can be seen to what extent the stress peaks are resolved by our numerical method at a resolution of 30 lattice-spacings over the cylinder diameter. Beyond $De=0.7$ we clearly lack spatial resolution. It is interesting to note that the consequences for not fully resolving this stress peak are not severe when it comes to capturing the way the drag force relates to the Deborah number (as earlier discussed in relation to Figure 3). As a final result regarding the two-dimensional cylinder-in-channel benchmark we assess in Figure 6 the effects of the finite extension length L^2 . It shows how the streamwise velocity profiles in the wake of the cylinder transit from near-Newtonian for $L^2 = 10$ to Oldroyd-B ($L^2 \rightarrow \infty$).

Spheres moving in viscoelastic liquids

We now turn to the actual subject of this paper which is motion of spherical particles in FENE-CR liquids. These involve intrinsically three-dimensional simulations with the particles moving relative to a fixed grid. For LB simulations of Newtonian liquids it has been recognized that having spherical particles on a cubic grid requires a calibration step [35]. Ladd [35] introduced the concept of a hydrodynamic diameter. The calibration involves placing a sphere with a given diameter d_{inp} in a fully periodic cubic domain in creeping flow and (computationally) measuring its drag force. The hydrodynamic diameter d of that sphere is the diameter for which the measured drag force corresponds to the expression for the drag force on a simple cubic array of spheres due to Sangani & Acrivos [36] which is a modification of the analytical expression due to Hasimoto [37]. Usually d is slightly bigger than d_{inp} with $d - d_{inp}$ typically equal to one

lattice spacing or less. For Newtonian fluids and a lattice-Boltzmann scheme the difference $d - d_{inp}$ is a weak function of the viscosity. For this reason, and given the non-Newtonian fluids dealt with in this paper the issue of hydrodynamic diameter needs careful consideration.

We first performed the Newtonian calibrations as described above. To assess how these calibrated spheres behave in an elastic liquid, they are placed in fully periodic domains, now containing a FENE-CR liquid with $\beta=0.1$ and $L^2 = 10$. The liquid is forced such that $Re=0.1$. Figure 7 shows how the normalized drag force F_d/F_d^N (with F_d^N the drag force at $\lambda=0$ and thus $De=0$) measured this way behaves as a function of Deborah number and spatial resolution; we compare calibrated spheres with $d=8, 12$ and 16 (lattice spacings Δ). We conclude that as long as $d \geq 12$ the drag results have an acceptably weak sensitivity to the spatial resolution: the maximum deviation in F_d/F_d^N obtained with $d=12$ and $d=16$ is less than 2%.

Rotation of a single sphere in shear flow

A relevant three-dimensional benchmark involves spherical particles subjected to simple shear flow. In Newtonian fluids under low inertia conditions the shear flow makes the sphere rotate at an angular velocity equal to half the shear rate. For the system and coordinates as defined in Figure 8 this means $\omega_y = \dot{\gamma}/2$ with $\dot{\gamma} = 2U_s/W$ the overall shear rate generated by two parallel plates moving opposite in the z -direction. Snijkers and co-workers [38,39] have experimentally and numerically investigated this system for a spectrum of elastic liquids and found a reduction of the ratio $\omega_y/\dot{\gamma}$ with the reduction getting stronger for higher Deborah numbers (here defined as $De = \lambda\dot{\gamma}$). In Figure 9 we show that our numerical method with a (modest) resolution such that the sphere diameter spans 12 lattice spacings ($d = 12\Delta$) is able to accurately reproduce the results in [39] for an Oldroyd-B liquid. The ratio $\omega_y/\dot{\gamma}$ decays monotonically with the Deborah number. The deviations between Snijkers et al's and our results are less than 4%. The curve in Figure 9 that we attribute to Snijkers et al has been derived from Figure 6 in their paper [39]. That

figure shows the ratio $\omega_y/\dot{\gamma}$ as a function of the Weissenberg (Wi) number for (among more) an Oldroyd-B liquid. For viscosity ratio $\beta = 0.5$, Wi is identical to De.

Sedimentation of a single sphere

Our numerical settling experiments will be performed in a cylindrical, closed container with square cross section (see Figure 10), and it is anticipated that wall effects significantly influence the settling velocities [40]. To benchmark this, we first report on the settling velocity of spheres in Newtonian liquids, where we assess the effect of blockage ratio $\text{Br} \equiv d/W$, and the effect of spatial resolution of the simulations. The parameters were chosen such that $\text{Re}_\infty \equiv \frac{\rho U_\infty d}{\mu} = 0.36$; the density ratio was $\frac{\rho_s}{\rho} = 2.5$. The calibrated spheres (see above for a discussion regarding hydrodynamic diameter calibration) are released at vertical location $z=0.8H$ (with $H=4W$) in the center of the cross section of the channel. They then quickly (within time $t = 0.5d/U_\infty$) attain a steady settling velocity. This steady velocity we report in Figure 11. The good agreement with the experimental data due to [40] demonstrates that the simulations correctly capture the dynamics of the system, including wall effects. Only minor effects of spatial resolution are observed.

In our study of spheres settling through elastic (FENE-CR) liquids, the main interest was the impact of the relaxation time on the dynamics of settling, i.e. the way the sphere starts up from rest and reaches a steady velocity. The effect of the relaxation time will be captured by the elasticity number

$\text{El} = \frac{\lambda\mu_0}{\rho d^2}$ that directly relates to input parameters of the simulations. The following non-dimensional

parameters were set to fixed values: the blockage ratio $\text{Br}=0.25$, the viscosity ratio $\beta=0.1$, the

(dimensionless) extension length $L^2 = 10$, the density ratio $\frac{\rho_s}{\rho} = 2.5$, and the aspect ratio $\frac{H}{W} = 10$.

Gravitational acceleration g was determined such that $\text{Re}_\infty \equiv \frac{\rho U_\infty d}{\mu_0} = 0.36$, with $U_\infty = \frac{(\rho_s - \rho)gd^2}{18\mu_0}$. In all

cases the resolution was such that the sphere diameter $d = 12\Delta$.

We first examine the transient behavior of the settling velocity; see Figure 12 (top panel). Elasticity is responsible for an initial overshoot of the settling velocity. This overshoot is followed by a strongly damped oscillation, with damping the result of viscous effects. The strength and the time-scale of the overshoot is a pronounced function of El . This dependency has been quantified by plotting the dimensionless time of the moment of maximum settling velocity t_p/λ against the elasticity number El (see Figure 12). A fit of the data points suggests that $t_p/\lambda \approx 0.6/\sqrt{El}$ with 0.6 a fitting parameter. Beyond dimensionless time $t/\lambda \approx 1$ the settling velocity gets steady with U/U_∞ increasing with increasing El , which implies drag reduction due to elastic effects [21,41]. The velocity quickly reducing to zero around $t/\lambda \approx 2.2$ for $El=11.11$ is the result of the sphere reaching the bottom of the container. It illustrates that for the parameter range studied the container is tall enough for the spheres to reach steady state, and the relatively short time over which the spheres decelerate from steady to zero velocity near the bottom.

For $El=5.56$ snapshots of flow structures are shown (in Figure 12, bottom panels) at characteristic moments in the time series. At the height of the overshoot we see a strongly for-aft-asymmetric flow. A flow region in the wake of the sphere with upward velocity (negative wake) has developed at the end of the deceleration that follows the overshoot. This is a stable structure as it remains intact after steady state has been reached [21,42].

Steady state flow around the settling sphere is examined in Figure 13 where we compare a non-elastic situation with two elastic cases. The negative wake is a clear characteristic of the latter with the negative wake approaching the sphere closer for higher elasticity number El .

Sedimentation of two spheres – Hydrodynamic interactions

To study hydrodynamic interactions between spheres in elastic liquids we place two spheres in a similar, square, tall container that we also used for the single-sphere study, and let them settle. The two types of initial placements of the spheres are given in Figure 14. In the vertical configuration both spheres start on the centerline of the container, with a distance s between their centers. The horizontal configuration is

made slightly asymmetric (with the initial midpoint between the spheres at $x=0.6W$ and $y=0.5W$) to enhance sphere-wall and (as a result) sphere-sphere hydrodynamic interactions. As for single sphere sedimentation, we focus on the effect of relaxation time λ (through the elasticity number); in addition we vary the initial spacing (in terms of the aspect ratio s/d) between the spheres. The rest of the dimensionless parameters were given fixed values: $Br = 0.25$, $H/W = 6$, $\beta = 0.1$, $L^2 = 10$, $\rho_s/\rho = 2.5$, and $Re_\infty = 0.36$.

We first discuss the results for the vertical configuration. For a Newtonian fluid and a vertical tandem configuration, in the moderate inertia regime ($0.25 < Re < 2.0$), the separation distance decreases with time as the spheres settle [15]. The stable steady configuration is a horizontal arrangement after the drafting-kissing-tumbling process [43]. In the low-inertia regime ($Re < 0.2$), the separation distance and spheres orientation remain constant [3]. Although in the present study $Re_\infty = 0.36$, the bounding walls sufficiently slow down the spheres to stabilize the vertical orientation of the pair of spheres settling in Newtonian liquid. The two spheres settle with the same velocity with the velocity slightly increasing for smaller spacing; see Figure 15.

In viscoelastic fluids, the necessary conditions for a stable vertical particle configuration were identified by Huang et. al. [44] as $\sqrt{Re \cdot De} < 1$ and $El > 1$. Under these conditions the nature of interaction (attraction or repulsion) between the two spheres depends on the initial separation distance [14,45]. For the complete range of initial separation distances considered, these authors reported an initial transient attraction. The transient attraction is followed by steady attraction or repulsion if their initial separation distance is less or greater than a critical value. This value depends on the fluid rheology and on the flow geometry.

The results of our systems are summarized in Figure 15 where we show time series of the spheres' vertical velocities and the separation distance starting from a zero-velocity, and zero-stress situation. Simulations of elastic liquids are compared with Newtonian ($El=0$) simulations, and the initial separation

distance has been varied. In all elastic cases we see an initial approach of the two spheres, followed by a separation. In the separation stage, the two spheres have virtually constant (though different) velocities.

The initial approach relates to a velocity overshoot that was also witnessed for a single sphere; the overshoot of the trailing sphere is larger than that of the leading one. The time-period of the overshoots is in agreement with that of a single sphere. The initial approach is consistent with the experimental observations of [14,15,45] and the two-dimensional and three-dimensional numerical calculations of [17,22]. The overshoot is followed by a rapid extension of the elastic fluid which generates a negative-wake behind the spheres as shown in Figure 16 (left panel). The negative wake of the leading sphere interacts with the trailing sphere and drives the spheres apart. This repulsion was not observed in the numerical studies [17] and [22]. In these papers, this was attributed to the absence of negative wakes. After the velocity overshoots for a second time, the two spheres reach a steady velocity.

The phenomena described above are clear functions of the levels of elasticity, and of the initial separation distance, as follows from comparing the results of the various cases as displayed in Figure 15. Higher elasticity and closer initial spacing lead to stronger sphere-sphere interactions.

In the horizontal side-by-side configuration of spheres (see Figure 14, right panel) we start with a slightly asymmetric placement (the midpoint between the sphere centers is $(x, y, z) = (0.6W, 0.5W, 0.8H)$). This is done to enhance lateral migration effects. It is known [46] for Newtonian fluids and at moderate Reynolds numbers ($0.1 < Re < 2.0$), that spheres settling side-by-side at close distance slowly move apart until an equilibrium separation distance is reached. Since this is a fairly slow process it would require very tall domains to mimic this computationally. By placing the spheres asymmetrically in the domain, lateral effects show up sooner and stronger and shorter domains can be applied. Only one initial placement and spacing ($s/d = 1.5$) was simulated; the variable in the simulations was the elasticity number El . The results are in Figures 17 and 18.

In addition to the earlier observations regarding velocity overshoot upon startup in elastic liquids, the most striking difference between the elastic cases and the Newtonian case is the repulsion of the two

spheres in the latter cases, and attraction in the former (see the middle panel of Figure 18). Also we see that the rate at which the two spheres change their mutual orientation from horizontal at startup to more inclined is a clear function of the elasticity number. This behavior is consistent with the experimental findings of Joseph et. al [15], two-dimensional numerical simulation of Feng et. al [17] and Stokesian dynamics simulation of Binous & Phillips [22].

Multiple spheres sedimentation

In this final Results subsection, the feasibility of simulations involving multiple spheres in a viscoelastic liquid has been investigated. These simulations will be compared with simulations involving a Newtonian liquid. Eight equally sized solid spheres (diameter d , spatial resolution such that $d=12\Delta$) are released in a tall, closed domain (no-slip walls all around) with square cross section (side length $W=4d$, and height $H=8W$). The solid over liquid density ratio is $\rho_s/\rho=2.5$ and the spheres sediment as a result of (net) gravity. The FENE-CR liquid has viscosity ratio $\beta=0.1$ and extension length parameter $L^2=10$. The total viscosity μ_0 and gravitational acceleration are such that $Re_\infty=0.36$. The elasticity number is $El=6.25$. The Newtonian liquid has a dynamic viscosity equal to the total viscosity of the FENE-CR liquid. Collisions between spheres are dealt with by means of a soft-sphere approach with a repulsive force between spheres that becomes active when the distance between two sphere centers gets less than $1.05d$. For collisions with container walls the spheres feel a wall-repulsive force when their centers got closer than $0.55d$ to a wall.

Two different initial conditions were considered. In the first one the spheres are placed symmetrically near the top of the container with their centers on the corners of an imaginary cube with side length $1.5d$. At this initial moment the spheres have zero velocity, and the liquid has zero velocity and zero stress. Compared to the first initial configuration, in the second the top four spheres are shifted in the positive x -direction by an amount $0.5d$; the bottom four by the same amount in the negative x -direction.

Symmetry is retained if the spheres are released in a symmetric arrangement (see the top row of panels in Figure 19). Initial repulsion between the spheres in the FENE-CR liquid is apparent. Where the

spheres in the Newtonian liquid reach a stable configuration in which their relative positions do not change anymore, the spheres in the viscoelastic liquid keep changing their mutual locations. With the asymmetric initial condition (lower row of panels in Figure 19) the spheres in Newtonian liquid tend to the same stable, symmetric configuration as when they were released symmetrically. This is certainly not the case with the elastic liquid. The level of asymmetry quickly grows in the course of the settling process. As noted above, vertical sphere configurations are stable if $\sqrt{\text{Re} \cdot \text{De}} < 1$ and $\text{El} > 1$ with Re and De based on the actual (average) sphere velocity U . The $\text{El} > 1$ condition is clearly met. Typically $U \approx 0.6U_\infty$ (as a result of the confinement) so that $\text{Re} = 0.216$. Since $\text{De} = \text{Re} \cdot \text{El}$, $\sqrt{\text{Re} \cdot \text{De}} \approx 0.54$. This would suggest that the spheres are evolving towards a vertical arrangement (if the container were sufficiently tall).

The computational effort involved in the eight-sphere simulations was not excessive. The total grid size was $48 \times 48 \times 384 \approx 0.9$ million lattice nodes. The simulations typically ran over 500,000 time steps. On a single CPU in modern hardware this took 252 hours (1.93 s per time step). The additional effort for solving the six transport equations of the components of the conformation tensor \mathbf{A} (Eq. 3) clearly shows if we compare runtimes for the FENE-CR liquid with those for the Newtonian liquid (1.93 s versus 0.68 s per time step). Given that the above is based on sequential computer code, and given the inherent parallel nature of the lattice-Boltzmann method we consider scaling up the computations to many more spheres in much bigger domains feasible. This would open up possibilities for simulations of dense solid-liquid suspensions involving elastic liquids.

Summary & outlook

A novel, direct simulation strategy for viscoelastic fluid flow has been developed. The simulation procedure solves the flow equations in the lattice-Boltzmann framework and the transport of elastic stress components using a finite volume scheme. Via an immersed boundary method, no-slip conditions on particles moving through the grid can be imposed. This allows for a tight coupling between the dynamics of the fluid and the solid: hydrodynamic forces and torques on the solid particles are resolved through the

immersed boundary method. These forces and torques are used to update the solids equations of (linear and rotational) motion that in turn provides boundary conditions for the liquid flow.

An important issue is that we apply a uniform, cubic computational grid, i.e. we do not use local grid refinement to (better) resolve regions in the flow with high gradients. This choice relates to our longer term goal to study dense suspensions involving many (order 1,000) particles moving relative to one another in viscoelastic liquids. For such simulations with so many particles adaptive grids are computationally unfeasible. At the same time we realize that the uniform grid at some locations under-resolves the flow. A main goal of the paper was to assess such resolution issues.

The assessment started with a two-dimensional benchmark: a planar Poiseuille flow of Oldroyd-B fluid over a cylinder placed in a channel where the surface of the cylinder was dealt with through the immersed boundary method. Compared with previous numerical work [33] drag coefficients were predicted within 3%. For moderate levels of elasticity (up to $De \approx 0.7$) and with a spatial resolution such that the cylinder diameter spanned 30 lattice spacings, the structure of the elastic stress field was represented adequately.

The three-dimensional simulations involved spherical particles moving through FENE-CR liquids. Where possible we compared with data from the literature. The reduction of the rotation rate relative to the shear rate of a sphere in simple shear flow when elasticity is increased [39] was resolved. For single settling spheres, velocity overshoot and negative wakes were reported. Hydrodynamic interactions between two spheres followed trends in accordance with experimental data [15]; where the strength and direction of interaction (attraction/repulsion) depends on the rheology of the liquid.

The feasibility of “many”-particle-simulations was demonstrated through simulations of eight settling spheres with (again) markedly different behavior in viscoelastic liquids compared to Newtonian liquids. In the eight-sphere-cases the particles were usually well separated and hardly collided. In dense suspensions they will be much closer to one another and could collide much more frequently. During the collision process the flow in the narrow spaces between spheres gets under-resolved. In the past this has

been dealt with by means of lubrication force modeling for suspension simulations with Newtonian liquids on fixed grids [7]. A similar strategy would need to be developed for viscoelastic liquids.

References

- [1] G.G. Stokes, *Mathematical and Physical Papers*, Volumes I-V, Cambridge University Press, Cambridge, 1901.
- [2] J.F. Richardson, W.N. Zaki, The sedimentation of a suspension of uniform spheres under conditions of viscous flow, *Chem. Engng. Sc.*, 8 (1954) 65.
- [3] G.K. Batchelor, Sedimentation in a dilute dispersion of spheres, *J. Fluid Mech.*, 52 (1972) 245.
- [4] A.J.C. Ladd, Effect of container walls on the velocity fluctuations of sedimenting spheres, *Phys. Rev. Lett.*, 88 (2002) 048301.
- [5] E. Guazzelli, J. Hinch, Fluctuations and instability in sedimentation, *Annu. Rev. Fluid Mech.*, 43 (2011), 97.
- [6] F. Lucci, A. Ferrante, S. Elghobashi, Modulation of isotropic turbulence by particles of Taylor length-scale size, *J. Fluid Mech.*, 650 (2010) 5.
- [7] J.J. Derksen, S. Sundaresan, Direct numerical simulations of dense suspensions: wave instabilities in liquid-fluidized beds, *J. Fluid Mech.*, 587 (2007) 303.
- [8] A. Ten Cate, C.H. Nieuwstad, J.J. Derksen, H.E.A. Van den Akker, PIV experiments and lattice-Boltzmann simulations on a single sphere settling under gravity, *Phys. Fluids* 14 (2002) 4012.
- [9] A. Ten Cate, J.J. Derksen, L.M. Portela, H.E.A. Van den Akker, Fully resolved simulations of colliding spheres in forced isotropic turbulence, *J. Fluid Mech.*, 519 (2004) 233.
- [10] J.J. Derksen, Simulations of granular bed erosion due to laminar shear flow near the critical Shields number, *Phys. Fluids*, 23 (2011) 113303.
- [11] J.J. Derksen, Direct numerical simulations of aggregation of monosized spherical particles in homogeneous isotropic turbulence, *AIChE J* (in press, 2011) DOI: 10.1002/aic.12761.
- [12] J.A. Somers, Direct simulation of fluid flow with cellular automata and the lattice-Boltzmann equation, *Appl. Sci. Res.*, 51 (1993) 127.

- [13] M.D. Chilcott, J.M. Rallison, Creeping flow of dilute polymer solutions past cylinders and spheres, *J. Non-Newton. Fluid Mech.*, 29 (1988) 381.
- [14] M.J. Riddle, C. Narvaez, R.B. Bird, Interactions between two spheres falling along their line of centers in a viscoelastic fluid, *J. Non-Newton. Fluid Mech.*, 2 (1977) 23.
- [15] D.D. Joseph, Y.J. Liu, M. Poletto, J. Feng, Aggregation and dispersion of spheres falling in viscoelastic liquids, *J. Non-Newton. Fluid Mech.*, 54 (1994) 45.
- [16] E.T.G Bot, M.A Hulsen, B.H.A.A van den Brule, The motion of two spheres falling along their line of centres in a Boger fluid, *J. Non-Newton. Fluid Mech.*, 79 (1998) 191.
- [17] J. Feng, P.Y. Huang, D.D. Joseph, Dynamic simulation of sedimentation of solid particles in an Oldroyd-B fluid, *J. Non-Newton. Fluid Mech.*, 63 (1996) 63.
- [18] J. Hao, T-W. Pan, R. Glowinski, D.D. Joseph, A fictitious domain/distributed Lagrange multiplier method for the particulate flow of Oldroyd-B fluids: A positive definiteness preserving approach, *J. Non-Newton. Fluid Mech.*, 156 (2009) 95.
- [19] Z. Yu, A. Wachs, Y. Peysson, Numerical simulation of particle sedimentation in shear-thinning fluids with a fictitious domain method, *J. Non-Newton. Fluid Mech.*, 136 (2006) 126.
- [20] P. Singh, D.D. Joseph, T.I. Hesla, R. Glowinski, T-W. Pan, A distributed Lagrange multiplier/fictitious domain method for viscoelastic particulate flows, *J. Non-Newton. Fluid Mech.*, 91 (2000) 165.
- [21] C. Bodart, M.J. Crochet, The time-dependent flow of a viscoelastic fluid around a sphere, *J. Non-Newton. Fluid Mech.*, 54 (1994) 303.
- [22] H. Binous, R.J. Phillips, Dynamic simulation of one and two particles sedimenting in viscoelastic suspensions of FENE dumbbells, *J. Non-Newton. Fluid Mech.*, 83 (1999) 93.
- [23] M.M. Villone, G. D'Avino, M.A. Hulsen, F. Greco, P.L. Maffettone, Simulations of viscoelasticity-induced focusing of particles in pressure-driven micro-slit flow, *J. Non-Newton. Fluid Mech.*, 166 (2011) 1396.

- [24] R.B. Bird, Dynamics of polymeric liquids, Wiley, New York, 1987.
- [25] O. Malaspinasa, N. Fiétier, M. Deville, Lattice Boltzmann method for the simulation of viscoelastic fluid flows, *J. Non-Newton. Fluid Mech.*, 165 (2010) 1637.
- [26] J.J. Derksen, Scalar mixing by granular particles, *AIChE J.*, 54 (2008) 1741.
- [27] J.H. Ferziger, M. Peric, Computational Methods for Fluid Dynamics, Springer, 2002.
- [28] S. Chen, G. D. Doolen, Lattice Boltzmann method for fluid flows, *Annu. Rev. Fluid Mech.*, 30 (1998) 329.
- [29] O. Shardt, S.K. Mitra, J.J. Derksen, Lattice Boltzmann simulations of pinched flow fractionation, *Chem. Engng. Sc.*, 75 (2012) 106.
- [30] D. Goldstein, R. Handler, L. Sirovich, Modeling a no-slip flow boundary with an external force field, *J. Comp. Phys.*, 105 (1993) 354.
- [31] J. Derksen, H.E.A. Van den Akker, Large-eddy simulations on the flow driven by a Rushton turbine, *AIChE J.*, 45 (1999) 209.
- [32] J.M. Verhelst, F.T.M. Nieuwstadt, Visco-elastic flow past circular cylinders mounted in a channel: experimental measurements of velocity and drag, *J. Non-Newtonian Fluid Mech.*, 116 (2004) 301.
- [33] M.A. Alves, F.T. Pinho, P.J. Oliveira, The flow of viscoelastic fluids past a cylinder: finite-volume high-resolution methods, *J. Non-Newton. Fluid Mech.*, 97 (2001) 207.
- [34] Y. Fan, R.I. Tanner, N. Phan-Thien, Galerkin/least-square finite-element methods for steady viscoelastic flows, *Journal of Non-Newton. Fluid Mech.*, 84 (1999) 233.
- [35] A.J.C. Ladd, Numerical simulations of particle suspensions via a discretized Boltzmann equation. Part I: Theoretical Foundation, *J. Fluid Mech.*, 271 (1994) 285.
- [36] A.S. Sangani, A. Acrivos, Slow flow through a periodic array of spheres, *Int. J. Multiphase Flow*, 8 (1982) 343.
- [37] H. Hasimoto, On the periodic fundamental solutions of the Stokes equations and their application to viscous flow past a cubic array of spheres, *J. Fluid Mech.*, 5 (1959) 317.

- [38] G. D'Avino, M.A. Hulsen, F. Snijkers, J. Vermant, F. Greco, P.L. Maffettone, Rotation of a sphere in a viscoelastic liquid subjected to shear flow. Part I: Simulation results, *J. Rheol.* 52 (2008) 1331.
- [39] F. Snijkers, G. D'Avino, P.L. Maffettone, F. Greco, M.A. Hulsen, J. Vermant, Effect of viscoelasticity on the rotation of a sphere in shear flow, *J. Non-Newton. Fluid Mech.*, 166 (2011) 363.
- [40] A. Miyamura, S. Iwasaki, T. Ishii, Experimental wall correction factors of single solid spheres in triangular and square cylinders and parallel plates, *Int. J. Multiphase Flow*, 7 (1981), 41.
- [41] J.V. Satrape, M.J. Crochet, Numerical simulation of the motion of a sphere in a boger fluid, *J. Non-Newton. Fluid Mech.*, 55 (1994) 91.
- [42] O.G. Harlen, The negative wake behind a sphere sedimenting through a viscoelastic fluid, *J. Non-Newton. Fluid Mech.*, 108 (2002) 411.
- [43] A. F. Fortes, D. D. Joseph and T. S. Lundgren, Nonlinear mechanics of fluidization of beds of spherical particles, *J. Fluid Mech.*, 177 (1987) 467.
- [44] P.Y. Huang, H.H. Hu and D.D. Joseph, Direct simulation of the sedimentation of elliptic particles in Oldroyd-B fluids, *J. Fluid Mech.*, 362 (1998) 297.
- [45] G. Gheissary, B.H.A.A. van den Brule, Unexpected phenomena observed in particle settling in non-Newtonian media, *J. Non-Newton. Fluid Mech.*, 67 (1996) 1.
- [46] J. Wu, R. Manasseh, Dynamics of dual-particles settling under gravity, *Int. J. Multiphase Flow*, 24 (1998) 1343.

Figure 1. Channel-with-cylinder geometry. At the left boundary a parabolic velocity profile is imposed. The aspect ratios are: $H = 4R = 2D$, $L_{ch} = 40R$, and $l = 10R$ (l runs from the inlet boundary to the center of the cylinder). The origin of the xz -coordinate system is in the center of the cylinder.

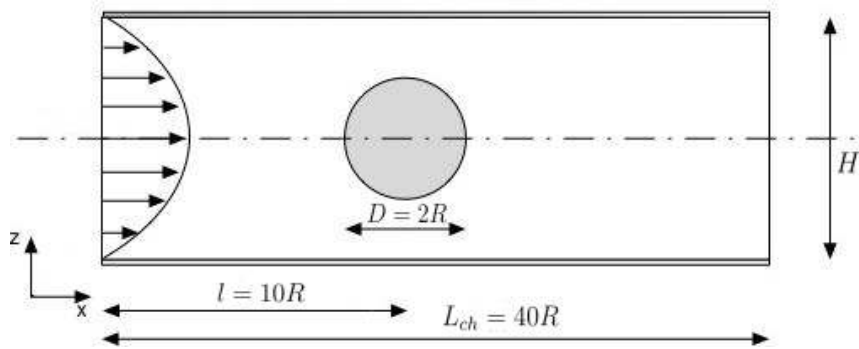


Figure 2. Velocity profiles on two grids M2 and M3. Top: streamwise velocity on the centerline downstream of the cylinder; bottom: streamwise velocity as a function of z at $x=0$. Newtonian fluid ($De=0$) and an Oldroyd-B fluid with $De = \frac{\lambda U}{R} = 0.9$ and viscosity ratio $\beta = \frac{\mu_s}{\mu_0} = 0.6$. For all cases

$$Re = \frac{\rho UR}{\mu_0} = 0.067.$$

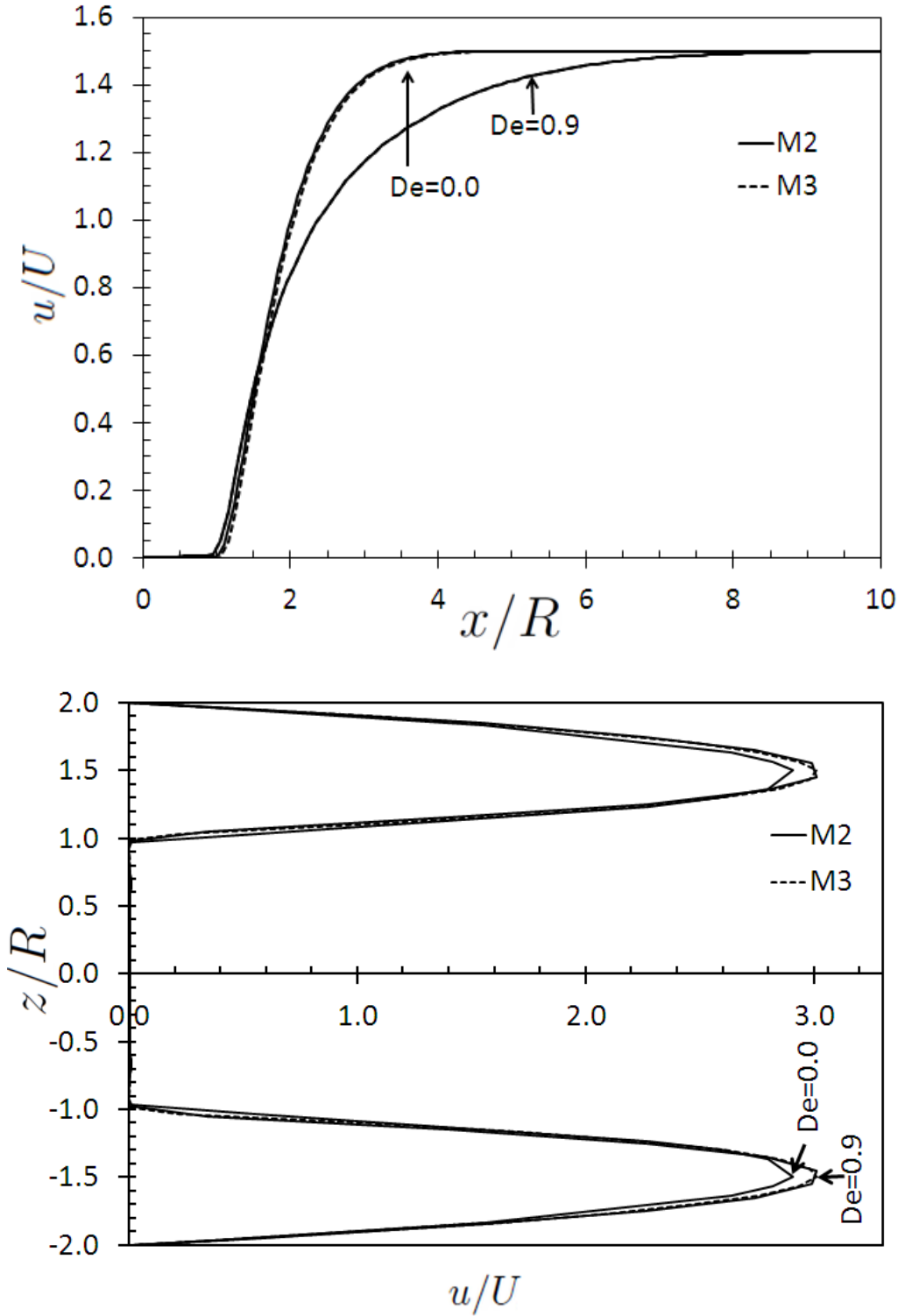


Figure 3. Drag coefficient $C_d \equiv \frac{F_d}{\mu_0 U}$ versus $De = \frac{\lambda U}{R}$ for an Oldroyd-B fluid; comparison with Alves et al [33]. Mesh M3, viscosity ratio $\beta = \frac{\mu_s}{\mu_0} = 0.6$, and $Re = \frac{\rho UR}{\mu_0} = 0.067$.

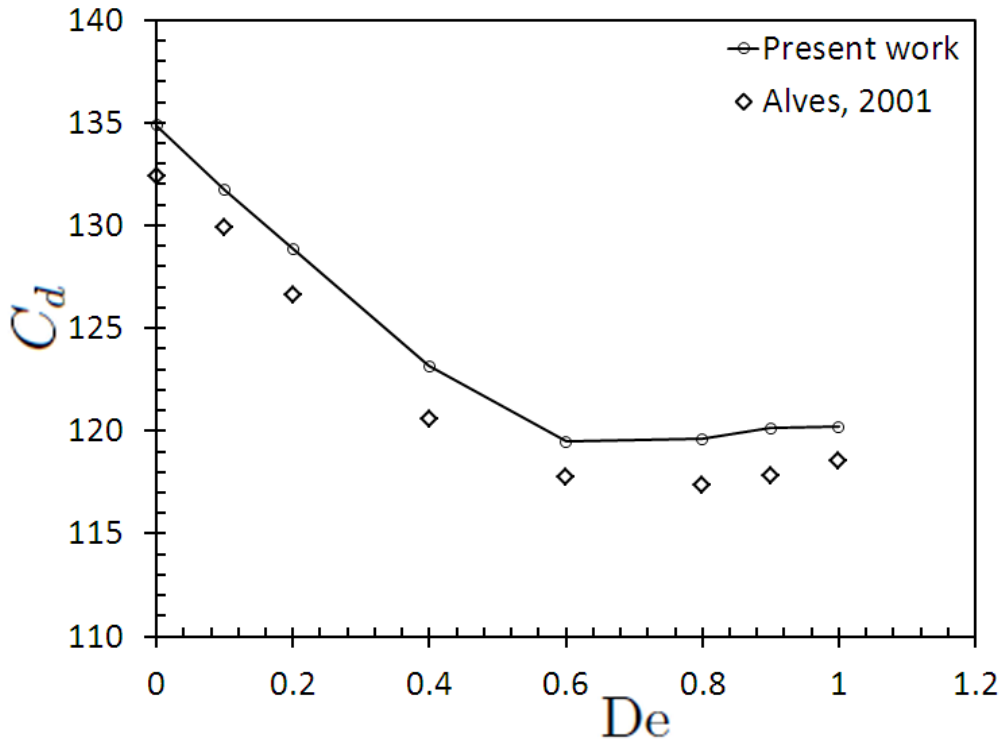


Figure 4. Streamwise velocity along the centerline of the channel for three Deborah numbers as indicated. Oldroyd-B fluids with viscosity ratio $\beta=0.6$. For all cases $Re = \frac{\rho UR}{\mu_0} = 0.067$. The symbols represent data due to Alves et al [33]; they have been sampled from the corresponding curves in their paper (their Figure 18).

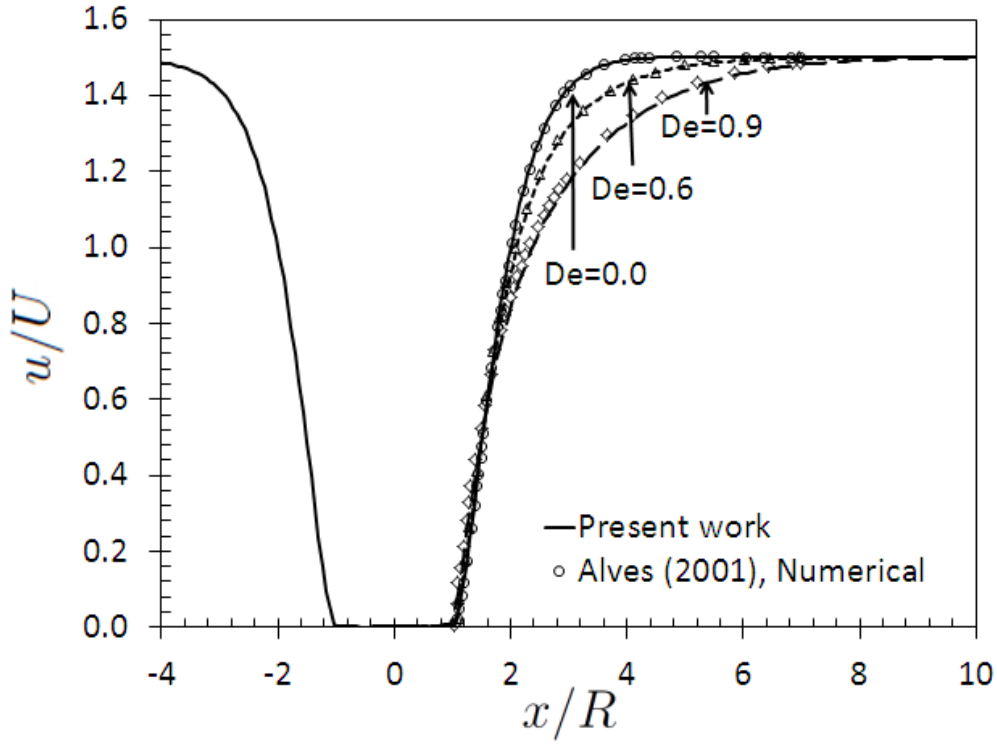


Figure 5. Streamwise normal elastic stresses (τ_{xx}^e). Top: contours for $De=1.0$; bottom: comparison with Alves et al [33]. Oldroyd-B fluids with viscosity ratio $\beta=0.6$ and $Re = \frac{\rho UR}{\mu_0} = 0.067$. The symbols in the bottom panel have been sampled from the corresponding curves in [33] (Figure 17 in [33]).

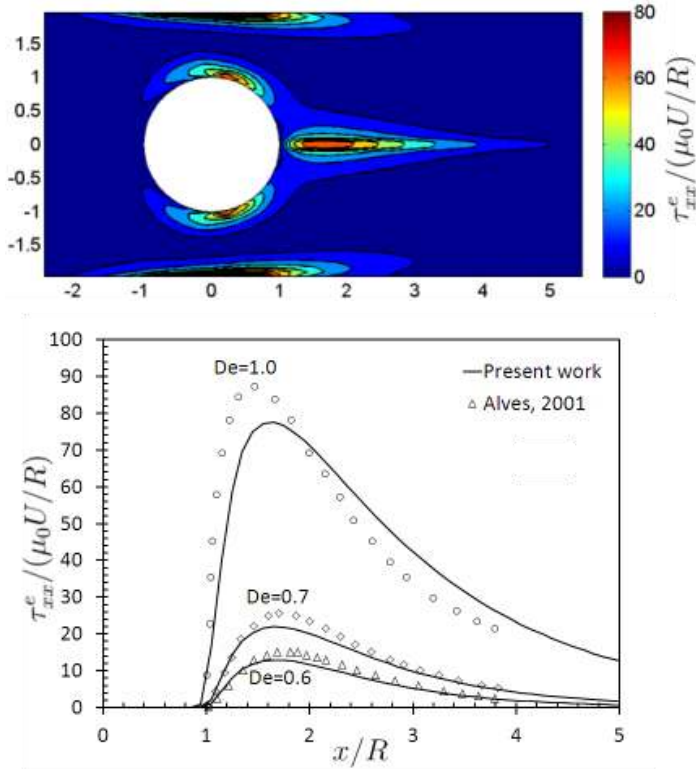


Figure 6. The effect of finite extension L^2 on the streamwise velocity in the wake of the cylinder; comparison between Newtonian, Oldroyd-B and FENE-CR liquids. Viscosity ratio $\beta = 0.6$, $De = 1.0$, and $Re = \frac{\rho UR}{\mu_0} = 0.067$.

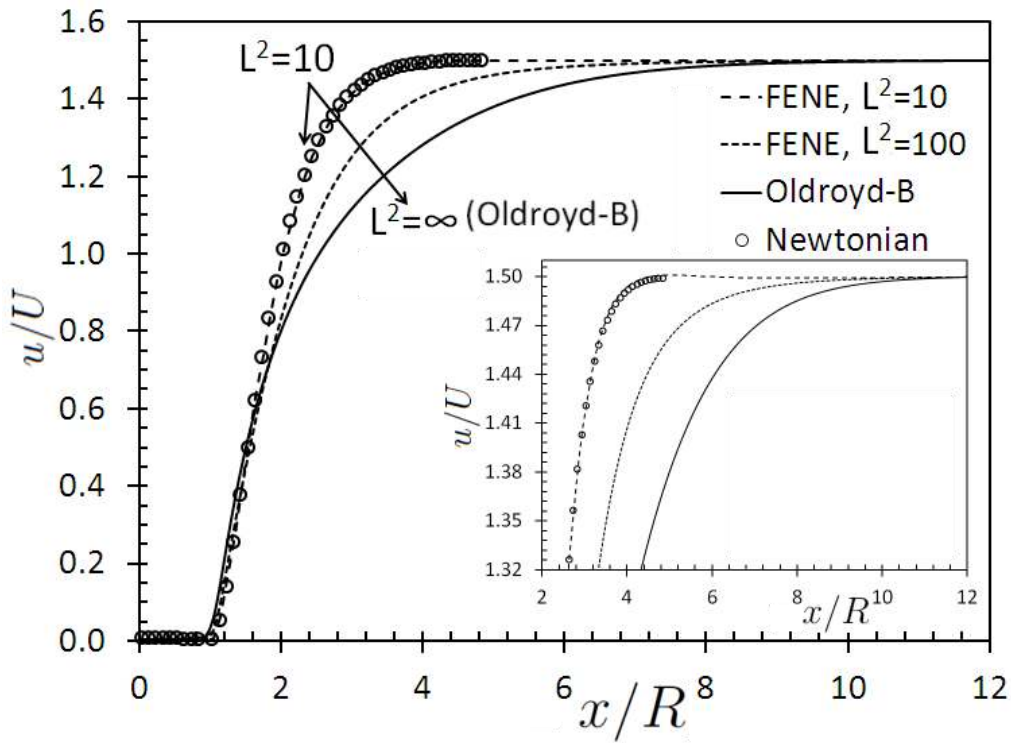


Figure 7. Steady state drag force on a sphere in a fully periodic, three-dimensional domain in a FENE-CR liquid; effect of De and spatial resolution. The drag force has been normalized with its Newtonian counterpart F_d^N . $\beta=0.1$, $L^2=10$, and $Re=0.1$.

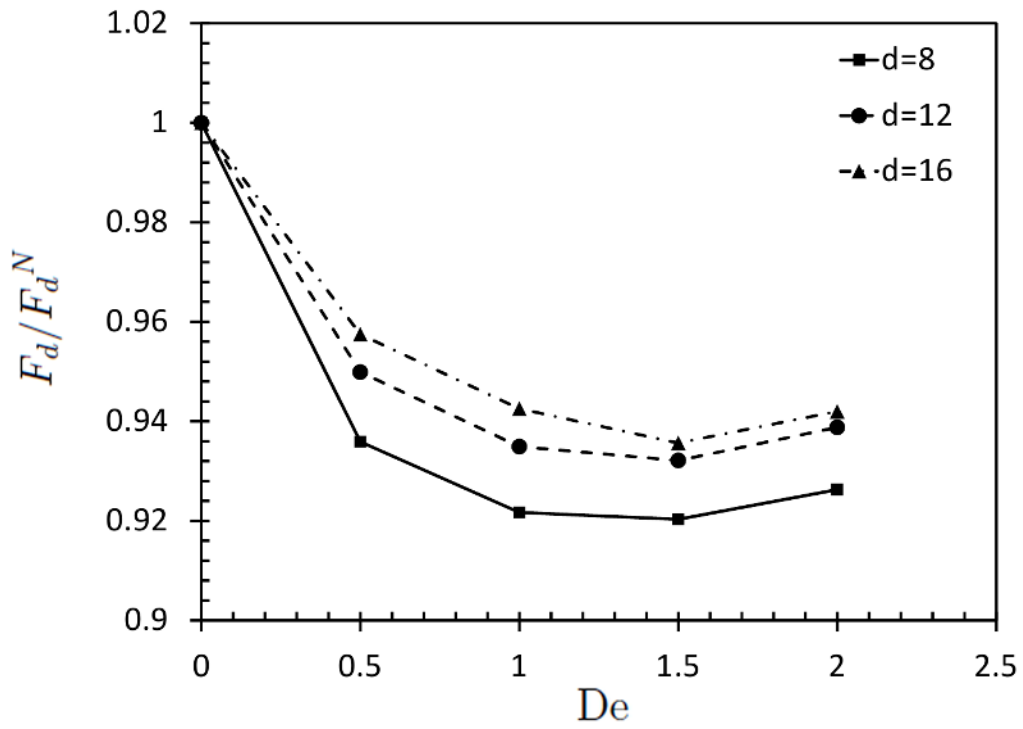


Figure 8. Sphere in shear flow geometry and coordinate definition. The flow is driven by two parallel plates at $x=0$ and $x=W$ moving in positive and negative z -direction respectively. The sphere is located in the center of the domain. Periodic conditions apply in y and z -direction. The blockage ratio is defined as $Br = d/W = 0.25$. The aspect ratio $H/W = 2$.

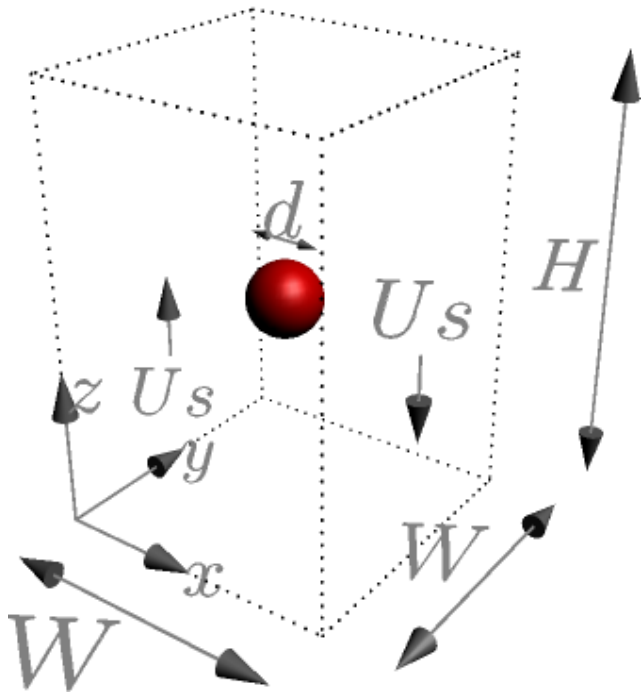


Figure 9. Sphere angular velocity ω_y as a function of De, comparison with Snijkers et al [39]. Oldroyd-B fluid. $Re \equiv \frac{\rho \dot{\gamma} d^2}{\mu_0} = 0.1$, $\beta = 0.5$, and $\rho_s / \rho = 2.5$.

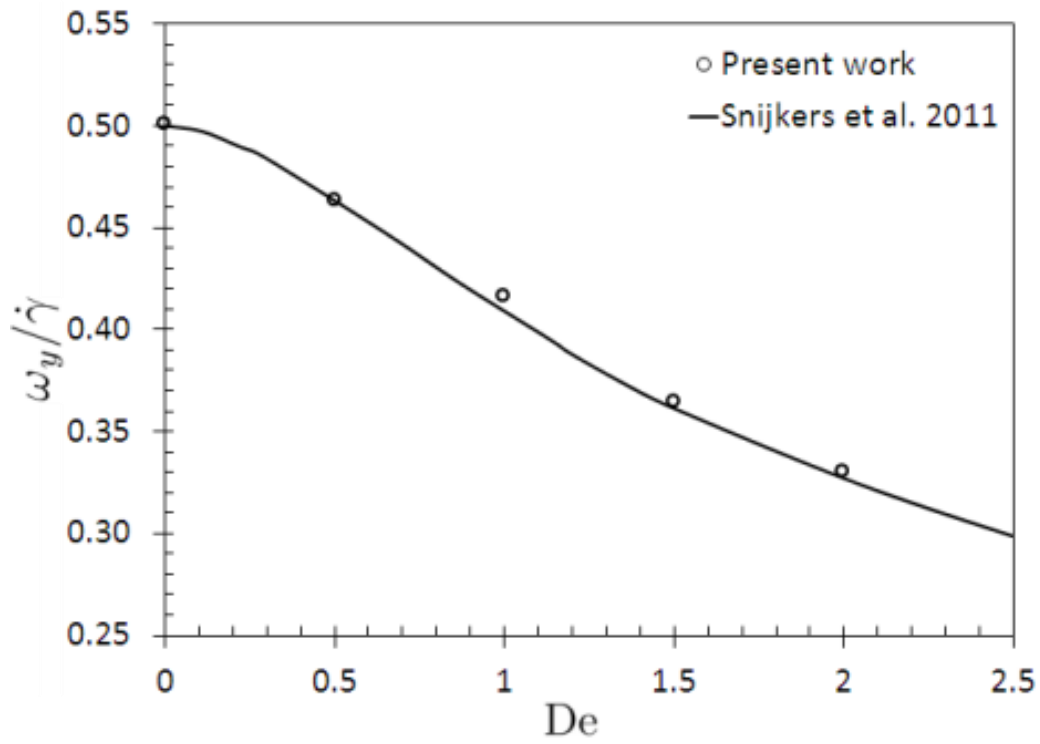


Figure 10. Single-sphere settling geometry, including coordinate system. No-slip conditions apply at all six bounding walls.

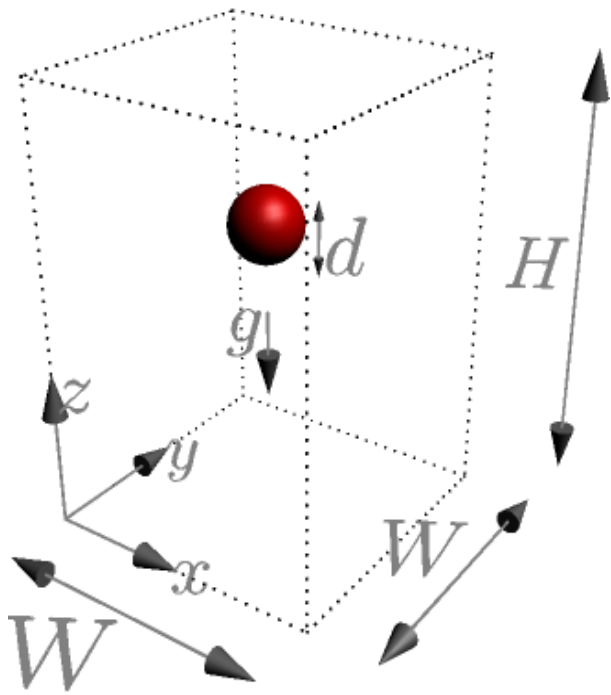


Figure 11. Single sphere settling through Newtonian liquid in a closed container with square cross section with side length W such that $Br = d/W$. Comparison with experiments of Miyamura et al [40], and assessment of grid sensitivity. $Re_\infty = 0.36$, $\frac{\rho_s}{\rho} = 2.5$.

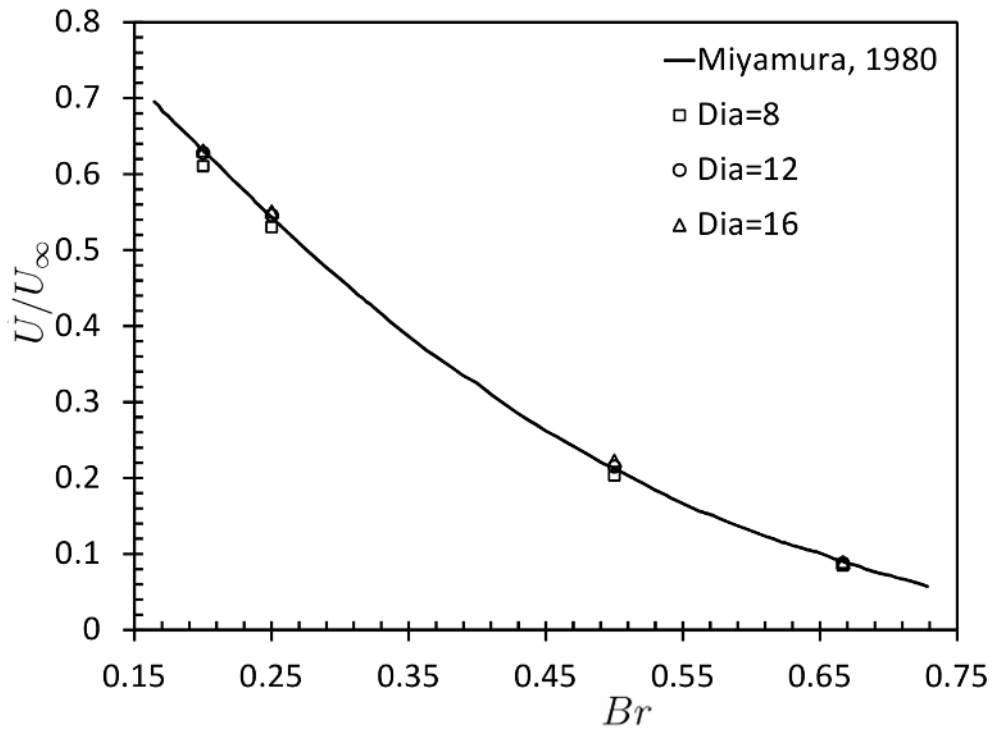


Figure 12. Top: time series of the settling velocity of a single sphere through FENE-CR liquids and (for reference) a Newtonian liquid. Time has been made non-dimensional with λ (and with d/U_∞ for the Newtonian case). The inset shows how the peak velocity instant t_p correlates with El . Bottom: streamlines for $El=5.56$ at three moments: from left to right $t/\lambda=0.2, 0.8,$ and 3.5 .

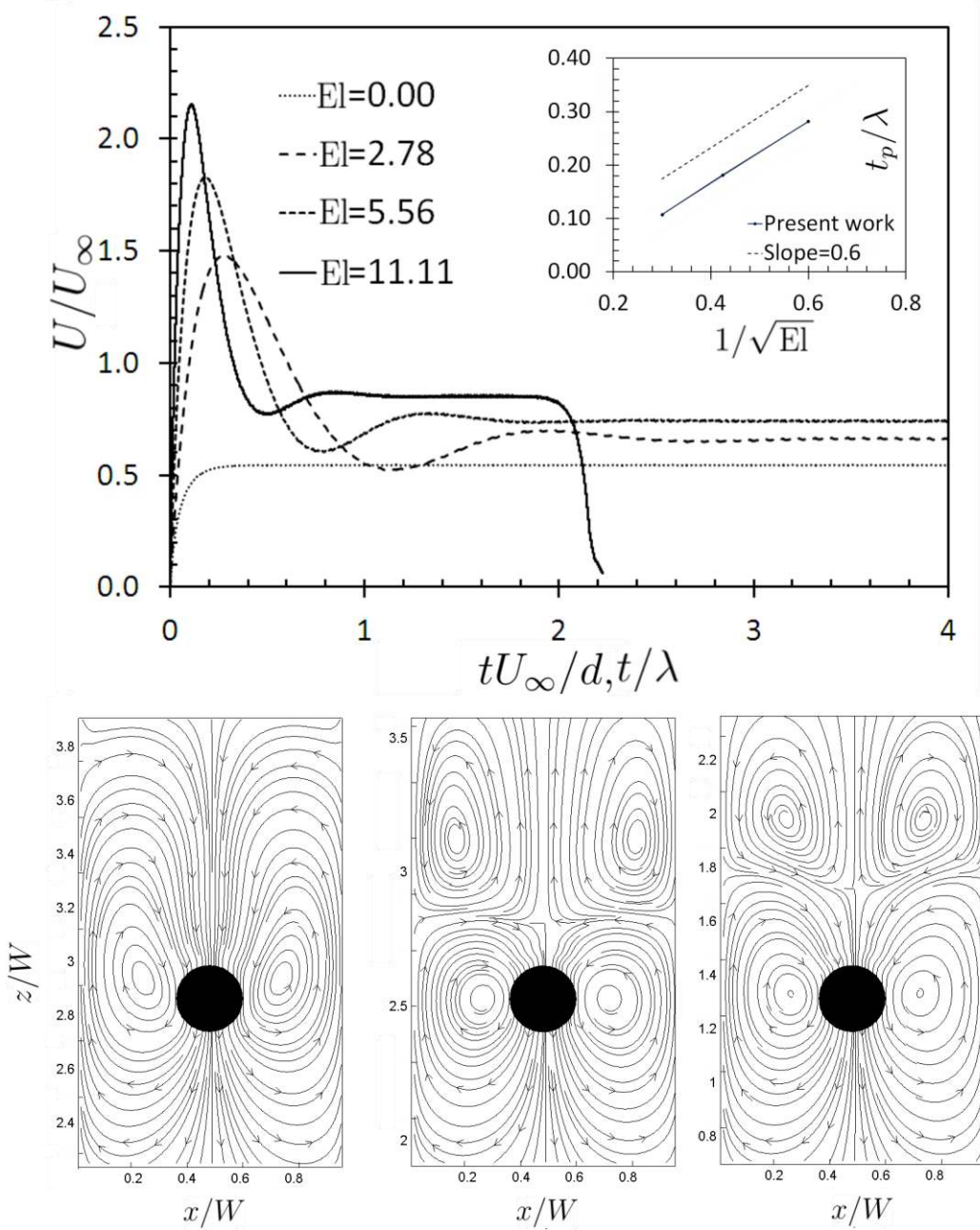


Figure 13. Streamlines around the settling sphere after steady state was reached for three different elasticity numbers: from left to right $El=0.0, 2.78, 5.56$.

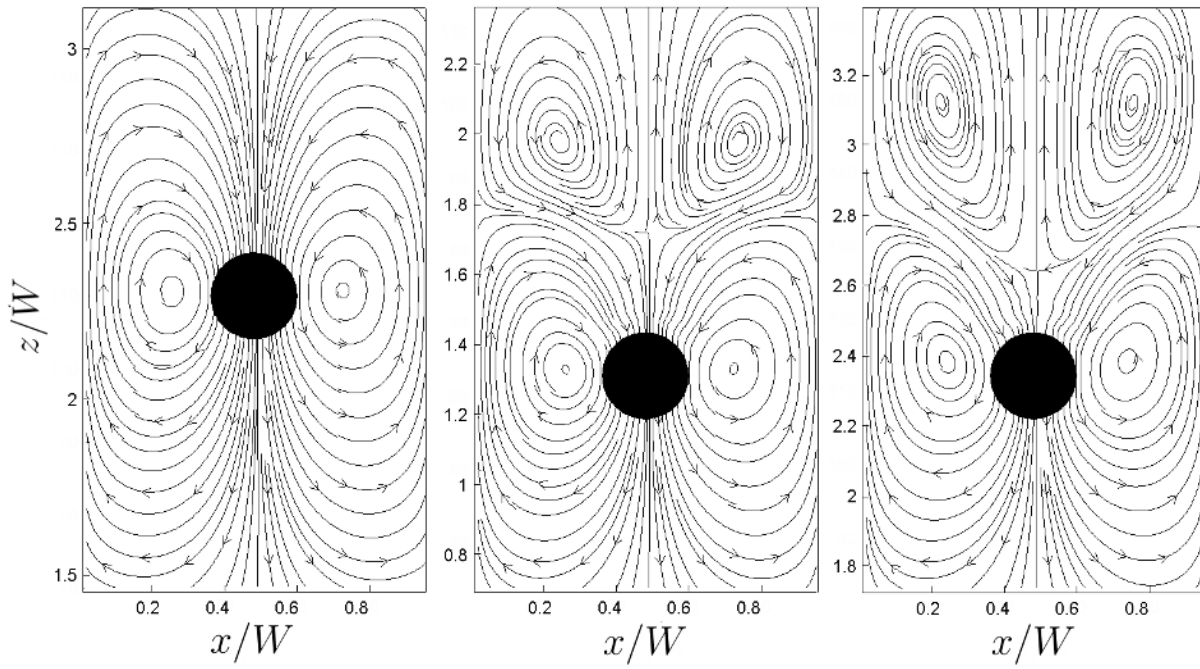


Figure 14. Two-spheres configurations. Left vertical orientation; right: side-by-side orientation. At the bounding walls, no slip conditions apply. The two spheres have the same diameter d . The starting positions are specified in the text.

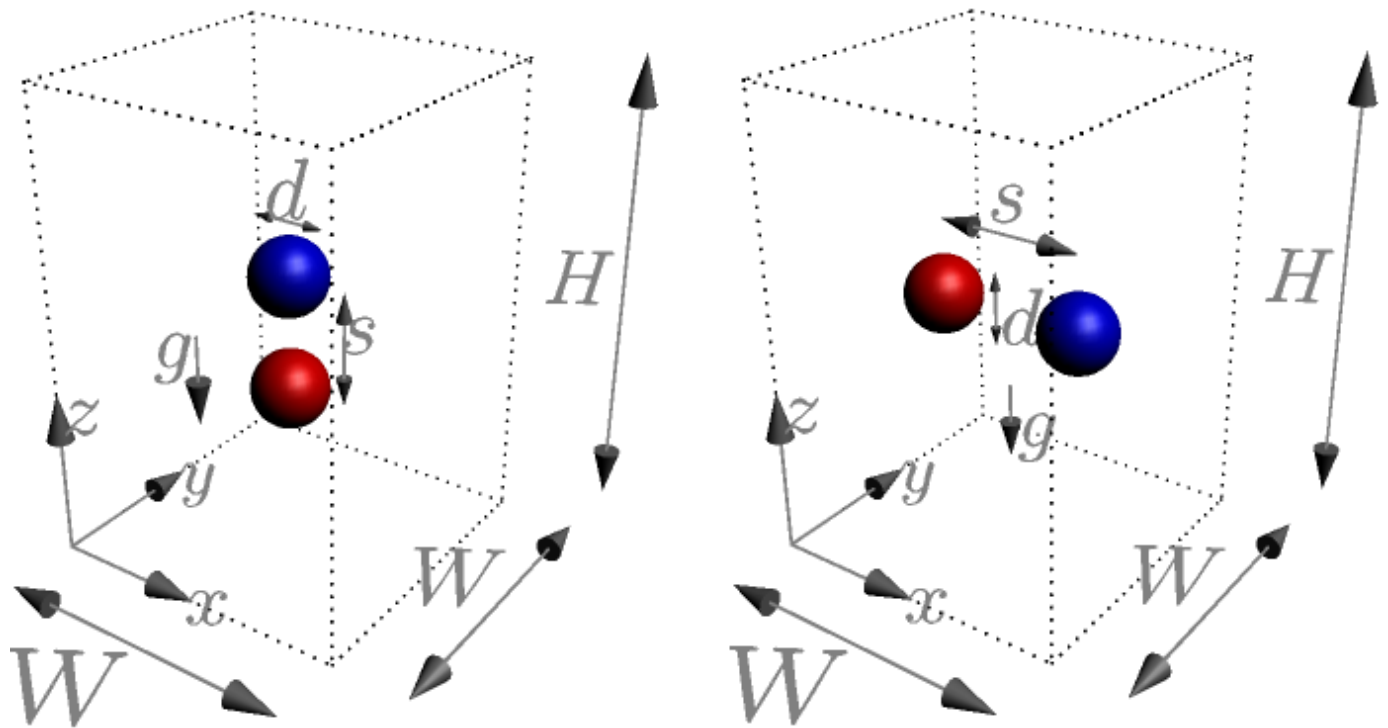


Figure 15. Time series of two spheres in vertical orientation settling over the centreline of the square container. Left column: velocities of the leading and trailing sphere for $El=4.17$ (and for Newtonian liquid for comparison). Right column: separation distance for three Elasticity numbers as indicated. From top to bottom: initial spacing between the two spheres $s/d = 1.5, 2.5,$ and 3.5 respectively. Time has been made non-dimensional with λ (and with d/U_∞ for the Newtonian cases).

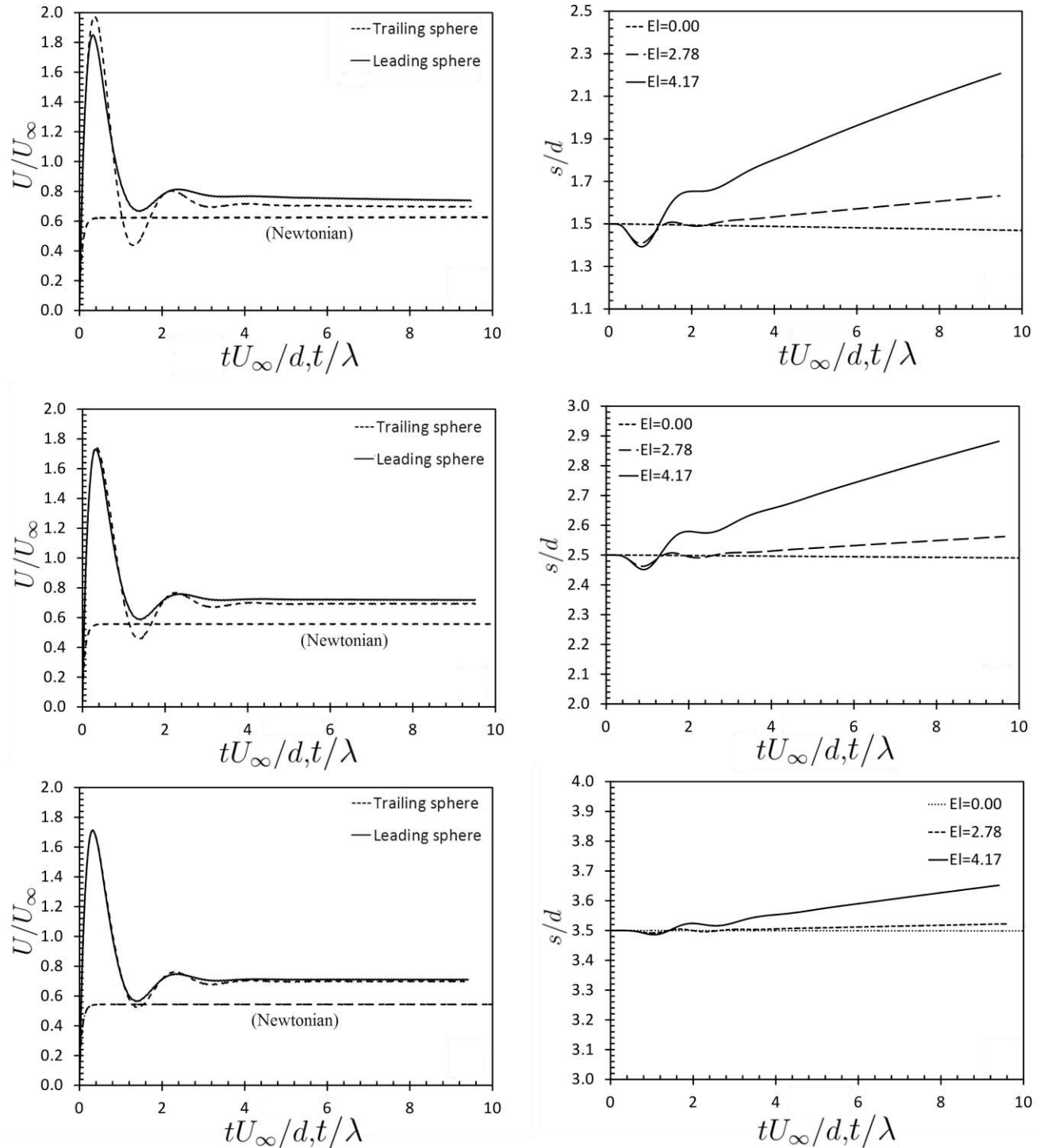


Figure 16. Two spheres in vertical orientation settling over the centerline of the square container with initial separation $s/d=1.5$ for $El=4.17$. From left to right $t/\lambda=0.4, 2.0,$ and 5.0 respectively. Streamlines and contours of $tr(\mathbf{A})$. The latter is a measure for elastic extension. Note that the color scale changes from panel to panel.

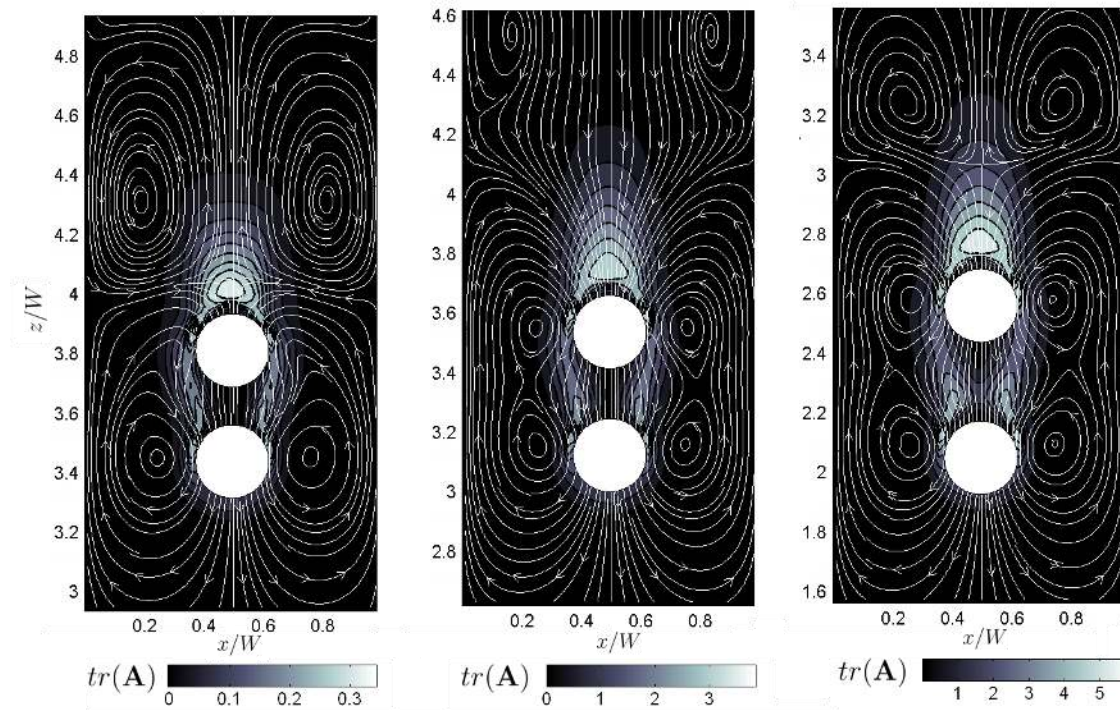


Figure 17. Two spheres settling side-by-side in a container with square cross section (width W , height $H=4W$). Slightly asymmetric starting position: the midpoint between the two spheres is at $(x, y, z) = (0.6W, 0.5W, 0.8H)$ for $t=0$. The initial spacing is $s/d = 1.5$. From left to right: $El=0.0, 2.08, 4.17, \text{ and } 6.26$. The subsequent spheres positions and orientations are spaced by $2.5d/U_\infty$ in time.

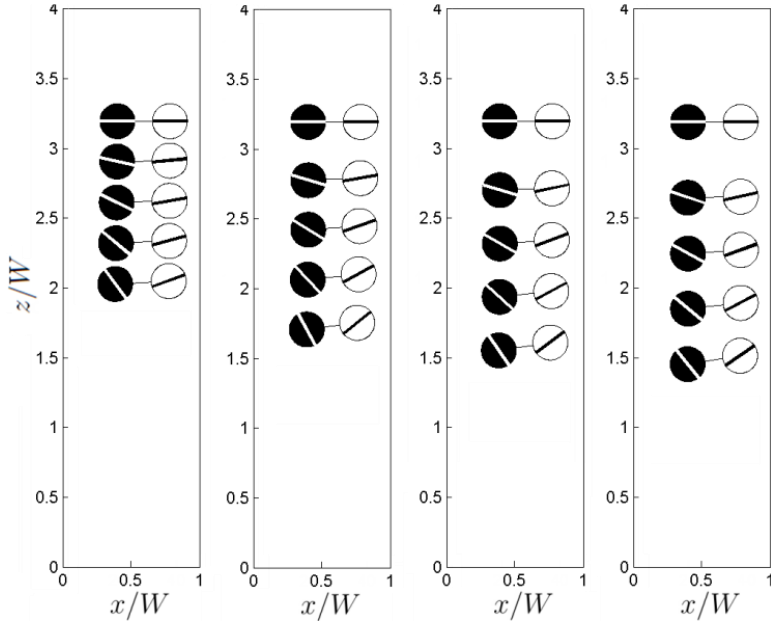


Figure 18. Time series of vertical velocities, horizontal spacing between the spheres and the y -component of the angular velocity for two spheres settling side-by-side in a FENE-CR liquid, and a Newtonian liquid. The initial spacing is $s/d = 1.5$; $El = 4.17$. The rest of the conditions have been specified in the text. Time has been made non-dimensional with λ (and with d/U_∞ for the Newtonian case).

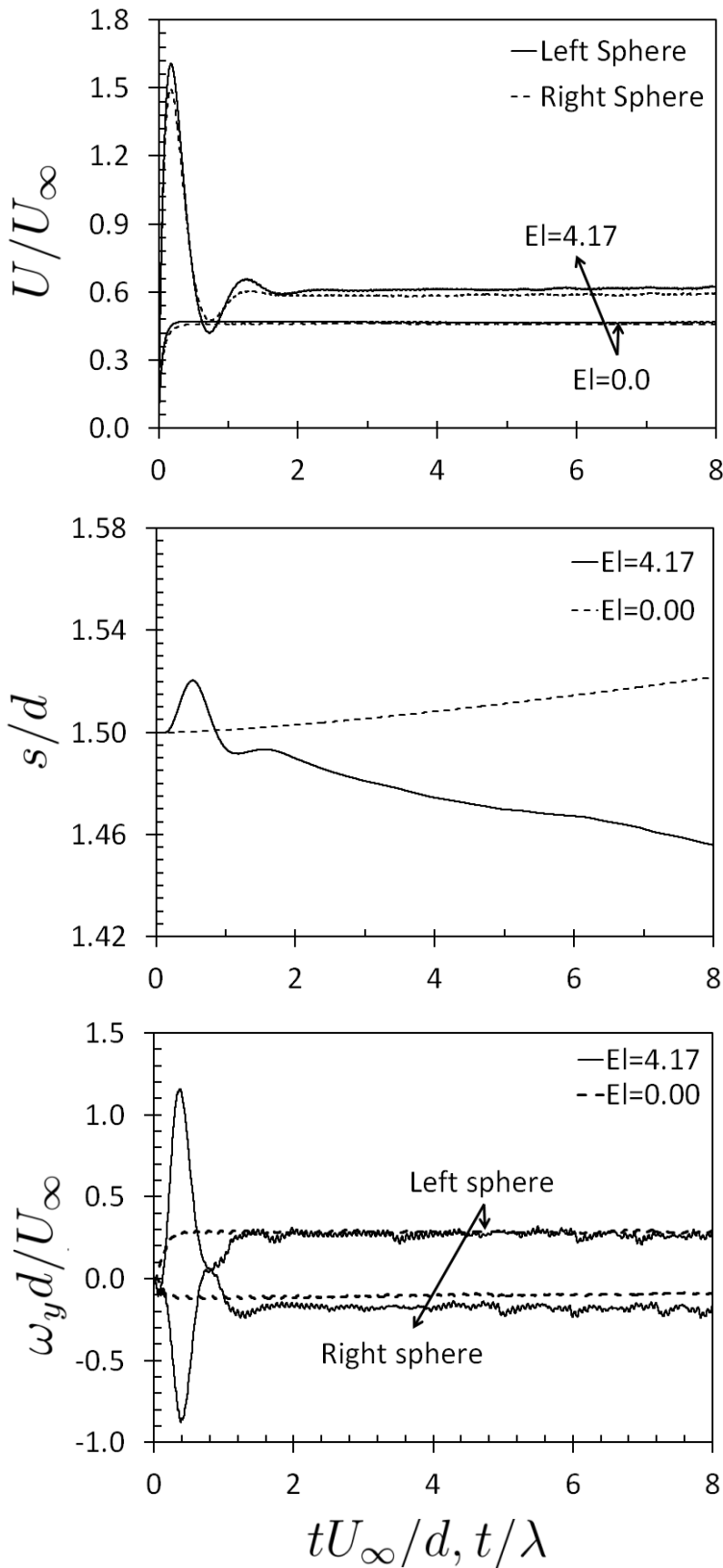


Figure 19. Eight solid spheres settling in a closed container with square cross section (width $W=4d$, height $H=8W$). Left: Newtonian liquid; right: FENE-CR liquid (specified in the text). The top and bottom panels differ with respect to the starting configuration of the spheres. For each of the four cases, four realizations are shown at times $\frac{tU_\infty}{d} = 0, 15, 30$ and 45 respectively. In addition the lower left sequence (Newtonian, asymmetric initial condition) shows a frame at $\frac{tU_\infty}{d} = 70$. In each frame one sphere is colored red for identification purposes only.

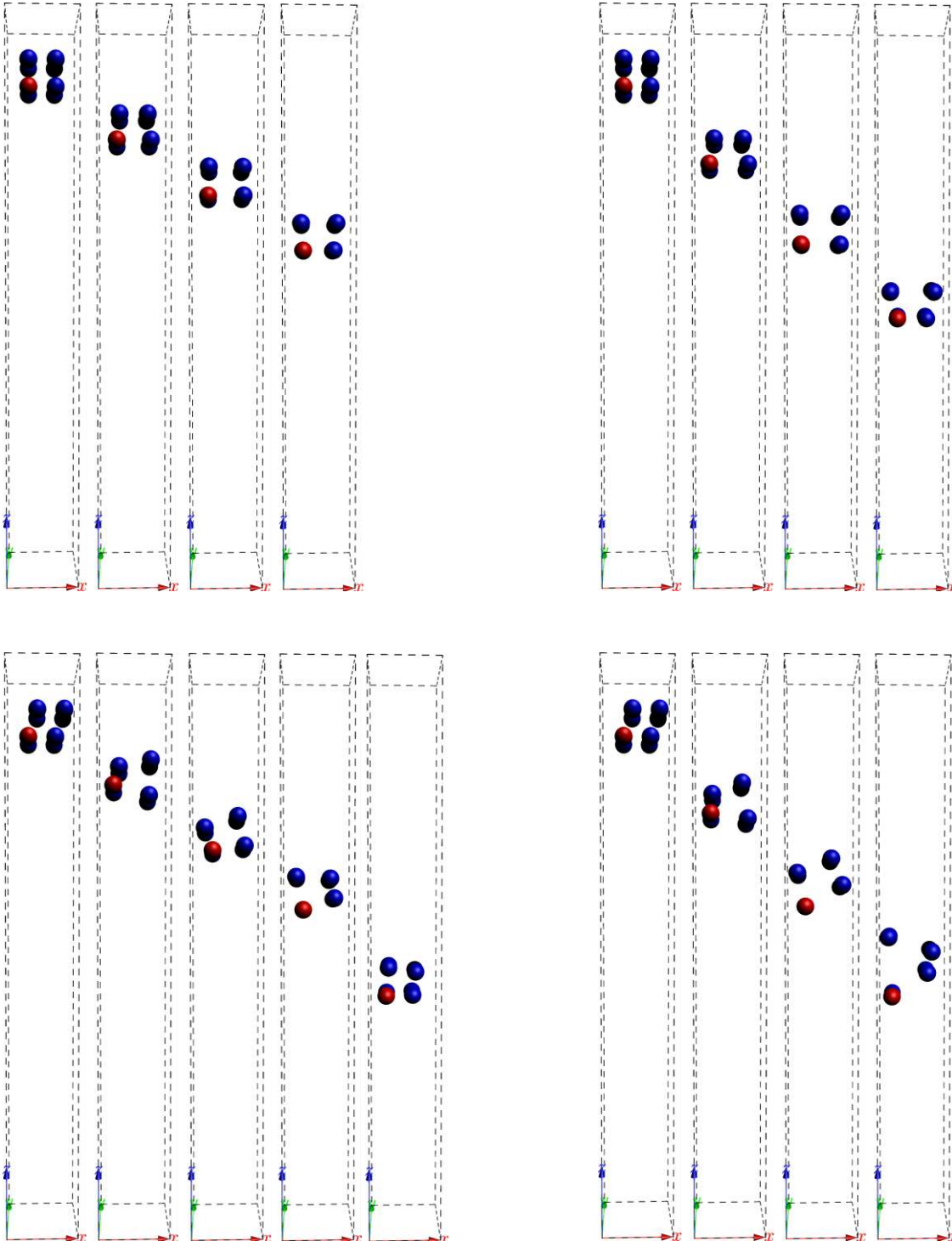


Table 1: Mesh sensitivity of drag force for Poiseuille flow of Oldroyd B fluid

De	C_d^{M1}	C_d^{M2}	C_d^{M3}	Alves et al [33]
0	145.22	136.50	134.87	132.36
0.1	139.80	133.20	131.73	129.91
0.2	136.83	130.31	128.85	126.62
0.4	133.85	125.04	123.15	120.59
0.6	131.52	121.77	119.49	117.77
0.8	133.35	121.95	119.61	117.36
0.9	134.45	122.55	120.12	117.85
1	136.28	123.18	120.20	118.52